IEEE Access
Multidisciplinary | Rapid Review | Open Access Journal

Received October 15, 2020, accepted October 24, 2020, date of publication October 27, 2020, date of current version November 11, 2020.

Digital Object Identifier 10.1109/ACCESS.2020.3034149

A PLL-Free Grid-Forming Control With Decoupled Functionalities for High-Power Transmission System Applications

TAOUFIK QORIA, EBRAHIM ROKROK, (Student Member, IEEE), ANTOINE BRUYERE, (Member, IEEE), BRUNO FRANÇOIS, (Senior Member, IEEE), AND XAVIER GUILLAUD, (Member, IEEE)

University of Lille, Arts et Metiers Institute of Technology, Centrale Lille, Yncrea Hauts-de-France, ULR 2697 - L2EP - Laboratoire d'Electrotechnique et d'Electronique de Puissance, 59000 Lille, France

Corresponding authors: Taoufik Qoria (taoufik.qoria@centralelille.fr) and Ebrahim Rokrok (ebrahim.rokrok@centralelille.fr)

This work was supported in part by the project HVDC Inertia Provision (HVDC Pro), financed by the ENERGIX program of the Research Council of Norway (RCN) under Project 268053/E2, and in part by the industry partners; Statnett, Statoil, Réseau de Transport de l'Electricité (RTE), and Elia.

ABSTRACT This paper proposes a grid-forming control strategy with a generic implementation approach to meet the transmission system requirements asking for the massive integration of power electronic devices into the power systems. In this context, several grid-forming controls have been proposed in the literature either with or without a Phase-Locked Loop (PLL). The PLL-based techniques allow decoupling the different control functionalities (i.e. inertia emulation, frequency support, active power setpoint tracking in steady-state) while the PLL-free schemes, which aim to avoid the PLL drawbacks, create a compulsory coupling between the control functionalities. The proposed grid-forming control in this paper is able to decouple the control functionalities without any dedicated PLL, which makes it more advantageous compared to what have been already proposed in the literature. Since the power converters are exposed to the small and large grid events, the presented control has been tested in both situations. For the small grid events, a simplified small-signal model is developed to assess the active power and frequency dynamics. In case of large grid events, a current limitation algorithm is included to the control in order to protect the power converter. To deal with the transient stability issues linked to the current limitation and enhance the converter performance during the post-fault, a method based on adaptive inertia constant is proposed. To validate the overall approach, time-domain simulations (in Matlab-Simulink) and experimentations are performed.

INDEX TERMS Active power regulation, current limitation, fast frequency response, grid-forming control, inertial effect, transient stability.

I. INTRODUCTION

The beginning of the renewable energy story had a moderate influence on the power electronic converters market. Very quickly, the connection of wind turbines and photovoltaic through power electronic converters became compulsory. In addition, some new transmission capacity had to be added in order to transmit the renewable energy from the place where it is generated to the place where it is consumed and also to improve the electricity market operation.

Today, a major share of the power electronic converters are controlled under the presumption that they are connected to a strong AC voltage with a given magnitude and frequency in such a way that the converter can simply inject a controlled power. This control strategy of the converter is well-known as the grid-following control. Grid-following converters have several limitations:

- Inability in stand-alone operation mode.
- Stability issues in connection to the weak grids and in faulty conditions [1], [2], which are mainly linked to the Phase-Locked Loop (PLL) dynamics and controllers interactions.
- The increase of grid-following converters results in the decrease of the total system inertia [3], [4].

To come up against these challenges, the way to control power converters has to be changed from following

The associate editor coordinating the review of this manuscript and approving it for publication was Zhouyang Ren.

the grid voltage to forming the grid voltage. Contrary to a grid-following converter that behaves as a current source, a grid-forming converter operates as a voltage source.

Unlike the grid-following control whose concept is quite well-accepted, the grid-forming control is still on debate and several variants (e.g. Virtual Synchronous Generator (VSG) [5]–[7], Synchronverter [8]–[12], Virtual Synchronous Machine (VSM) [13]–[19], VISMA [20] and droop control with lead-lag unit [5], [21]) are proposed in the literature. All these concepts adopt the idea of controlling the converter to mimic an actual Synchronous Machine (SM) [22], [23]. Other control laws allowing the grid-forming capability have been proposed recently: Virtual Oscillator (VOC) [24]–[29], matching control [30] and Inducverter [31]. It has been proved that the VOC is equivalent to a conventional droop control from a small-signal point of view [25], [26], [32]. However, this control may be more advantageous in case of voltage unbalance and distortion due to its non-linear characteristic [25], [29]. The matching control is another method to emulate the SM's behavior by creating a link between the DC bus voltage and the frequency at the AC side through the control. The main drawback of such controller is the all-in-one feature. It means that the DC voltage control, grid-frequency control, power sharing and the active power control are managed with only one control gain that prevents optimizing all these functionalities at the same time.

Some of these controllers such as VSG and VSM use a PLL to decouple the power control from the frequency control capability. Whereas, the droop control, virtual oscillator, matching control, Inducverter are not using a PLL. Actually the PLL-free controls are preferred to avoid the numerous stability issues caused by the PLL [33], [34] and possible interaction between the PLL modes and power controller modes [35]. However, with these control techniques, a coupling between the different control functionalities has been noticed. In case of a grid frequency variation these controllers cannot guarantee the steady state active power tracking because of the inherent frequency support function, which is induced by these types of grid-forming control [33].

To the best of our knowledge, until now, no control technique that allows decoupling the control functionalities without any dedicated PLL has been proposed. This decoupling is very important since the owner of the power electronic device can decide if the converter participates to primary frequency support or not.

In this paper, a grid-forming control scheme embedding the decoupled capabilities is developed. The proposed control is PLL-free. It is demonstrated that it meets the main requirements of a large transmission system such as inertial effect, good robustness in case of a grid impedance variation, and management of the voltage at the Point of Common Coupling (PCC). It is also shown that with a simple modification on the inertia constant during a fault, this control reveals a good transient stability. The contributions of the paper are listed as follow:

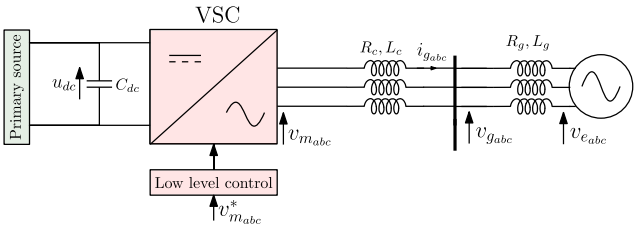

FIGURE 1. Generic topology of the VSC.

1) A new grid-forming control scheme with the ability to decouple different control functionalities without a dedicated PLL.
2) Simplified theoretical models to analyze the dynamic behavior of the system. Time-domain simulations support these models.
3) A generic approach for the implementation of the proposed grid-forming control scheme on a 2-level VSC by including all the control functionalities; specifically current limitation algorithms.
4) A method based on an adaptive inertia constant to improve the transient stability of the implemented grid-forming control.

To prove the effectiveness of the proposed control, different test cases with a 5kW small-scale experimental platform under normal and abnormal conditions have been tested.

The remaining of this paper is organized as follows. Section II presents the origin of the grid-forming control and introduces the controller, which drives the angle of the voltage modulated by the converter. In section III, the full implementation of the grid-forming control on a 2-level VSC is explained. Section IV is devoted to the analysis of the active power and frequency dynamics around an operating point with the implemented control. In section V, the transient stability issue is addressed and a method to enhance the stability is proposed. The experimental validation of the proposed control is given in section VI. Finally, section VII concludes the paper.

II. BASICS ON THE GRID-FORMING CONTROL

The main aim of a Voltage Source Converter (VSC) is to convert an AC power to a DC power and vice-versa. In what follows, the VSC is assimilated to a controllable three-phase voltage source: v_{m_a}, v_{m_b}, v_{m_c}, which are modulated from a DC bus voltage. The control system defines a set of three-phase signals $v^*_{m_a}$, $v^*_{m_b}$, $v^*_{m_c}$, in such a way that the average values of v_{m_a}, v_{m_b}, v_{m_c} during the switching time of the transistors are equal to the corresponding reference signals (see Fig. 1).

Some assumptions are made to simplify the analysis:

- It is supposed that the VSC is connected to the grid with a transformer, which is modeled with its series impedance $R_c + jX_c$. In the first step, the $L_f C_f$ filter that is usually used for 2- Level VSCs is neglected in order to simplify the analysis.

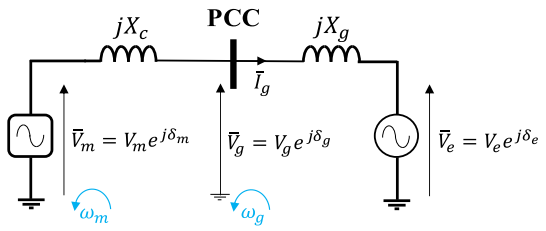

FIGURE 2. Single-phase quasi-static representation of the VSC connected to the grid.

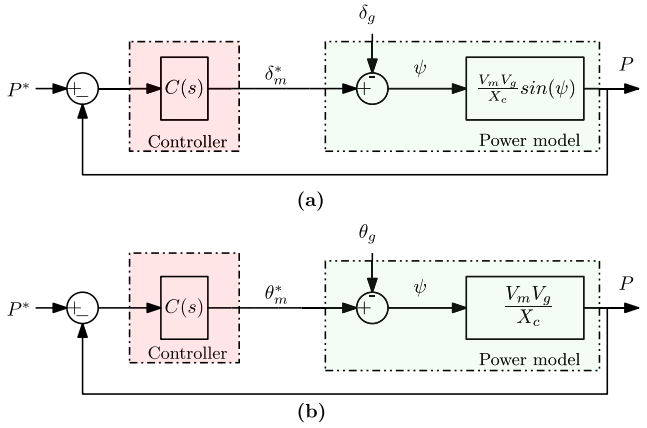

FIGURE 3. Active power control: (a) phasor representation (b) EMT representation.

- The converter is connected to a power transmission system, and therefore, the resistance is much smaller than the reactance.
- The grid is modeled by a Thevenin equivalent composed of a voltage source $v_{e_{abc}}$, an inductance L_g and a resistance R_g.

A. ACTIVE POWER CONTROL WITH THE MODULATED VOLTAGE ANGLE

The general organization of the active power control in a grid-forming converter can be explained with some simple considerations based on a quasi-static model of the grid described in Fig. 2.

The injected active power by the power converter in per-unit can be expressed as follows:

$$P = \frac{V_m V_g}{X_c} sin\left(\psi\right), \quad \psi = \delta_m - \delta_g, \tag{1}$$

where V_m and V_g are the RMS values of the modulated voltage and the PCC voltage, respectively. The angles δ_m and δ_m are the corresponding phasor angles. The base power S_{b_1} is equal to the nominal power of the converter.

Since it is not possible to control a difference of angles, the effective control signal is δ_m. Fig. 3-a shows a general scheme for the active power control. The output of the control is δ_m^*, a reference angle for δ_m. Fig. 3-a presents also a quasi-static system model.

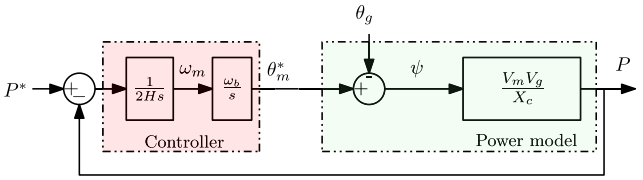

FIGURE 4. Power control with a double integrator.

In the real life, the control is implemented in the time domain. Let's define ω_m, the modulated voltage angular frequency (in per-unit) and ω_g, the frequency at the PCC. ω_b is the base frequency in rad/s. θ_m and θ_g are the time-domain angles for the modulated voltage and the PCC voltage v_g, respectively. It results in:

$$\theta_m(t) = \omega_m \omega_b t + \delta_m, \tag{2}$$

$$\theta_g(t) = \omega_g \omega_b t + \delta_g. \tag{3}$$

The Electromagnetic Transient (EMT) implementation of the active power control is illustrated in Fig. 3-b where ψ is supposed to be small enough so that $sin(\psi) \approx \psi$.

Several types of controller can be chosen to control the active power. Since the disturbance θ_g is linearly varying with the time in steady state, a simple integrator is not enough to cancel the error between the active power and its reference [32]. A double integrator is able to cancel this difference in steady state (Fig. 4). Moreover, it brings an inertial effect since it induces a proportional relation between the power variation and the derivative of the frequency ω_m:

$$\Delta P = P^*\left(t\right) - P\left(t\right) = \frac{2H}{\omega_b} \frac{d^2\theta_m}{dt^2} = 2H \frac{d\omega_m}{dt}. \tag{4}$$

This equation is similar to the swing equation in a synchronous machine where, in per unit, the torque variation is nearly equal to the power variation. From the block diagram shown in Fig. 4, it is possible to calculate P with respect to P^* and θ_g:

$$P = \frac{1}{\frac{2H}{\omega_b K_c} s^2 + 1} P^* - \frac{\frac{2H}{\omega_b} s^2}{\frac{2H}{\omega_b K_c} s^2 + 1} \theta_g, \tag{5}$$

where $K_c = V_m V_g / X_c$. Equation (5) shows that this system is an oscillator. A damping effect has to be added to bring an acceptable dynamic behavior.

B. PROPORTIONNAL AND INTEGRAL ACTION TO GENERATE THE INTERNAL ANGLE

A proportional action k_p on the active power can be added to damp the oscillation as depicted in Fig. 5. It results in a specific formulation of the PI controller, called IP controller in this paper. The active power transfer function is expressed as follows:

$$P = \frac{1}{\frac{2H}{\omega_b K_c} s^2 + 2Hk_p s + 1} P^* - \frac{\frac{2H}{\omega_b} s^2}{\frac{2H}{\omega_b K_c} s^2 + 2Hk_p s + 1} \theta_g. \tag{6}$$

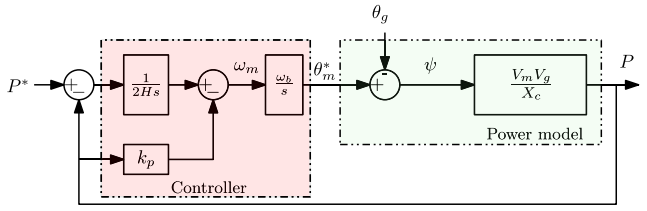

FIGURE 5. Proposed scheme with an IP controller.

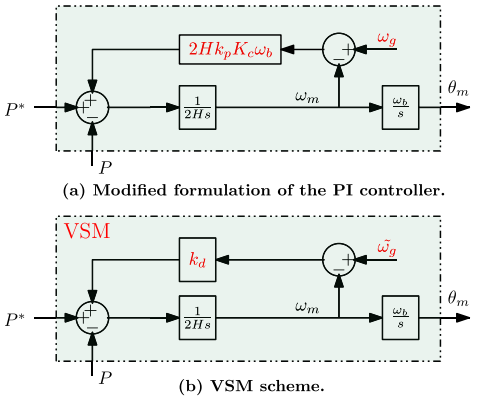

FIGURE 6. Equivalence between VSM and PI-controller.

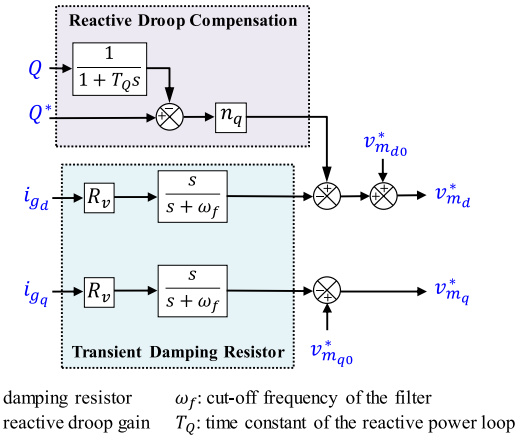

FIGURE 7. Scheme for generation of the reference voltage magnitude.

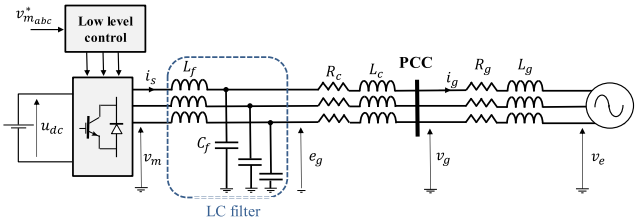

FIGURE 8. A 2-Level VSC with an LC filter connected to the grid.

The gain k_p is calculated with respect to a specific damping coefficient ζ. From the original formulation, it is possible to modify the scheme proposed in Fig. 5 in order to reveal a "Virtual Synchronous Machine" like formulation. Indeed, from (1), it can be deduced that:

$$P = \frac{V_m V_g}{X_c} \frac{(\omega_m - \omega_g)\,\omega_b}{s} = K_c \frac{(\omega_m - \omega_g)\,\omega_b}{s}. \tag{7}$$

The internal frequency from the proposed control depicted in Fig. 5 is expressed as:

$$\omega_m = \frac{1}{2Hs}\left(P^* - P\right) - k_p P. \tag{8}$$

Replacing the term $k_p P$ in (8) by (7) yields:

$$\omega_m = \frac{1}{2Hs}\left(P^* - P\right) - \frac{k_p K_c(\omega_m - \omega_g)\omega_b}{s}. \tag{9}$$

Equation (9) can be re-written as follows:

$$2Hs.\omega_m = \left(P^* - P\right) + 2Hk_pK_c(\omega_g - \omega_m)\omega_b. \tag{10}$$

This new mathematical formulation of the internal frequency is graphically illustrated in Fig. 6-a. It has to be emphasized that this control cannot be implemented like that. It is just another way to present the control in order to show its similarity with the VSM presented in Fig. 6-b. Although the general organization is similar, there is a fundamental difference since the estimation of the grid frequency $\tilde{\omega_g}$ needed in the VSM [18] is replaced with the grid frequency ω_g itself.

C. GENERATION OF REFERENCE VOLTAGE MAGNITUDE

The second constituent of the grid forming control is the management of the voltage magnitude. In steady state its reference is determined by the given setpoints $v^*_{m_{d_0}}$ and $v^*_{m_{q_0}}$ as illustrated in Fig. 7. When choosing to align the voltage with the d-axis, then $v^*_{m_{q_0}}$ is set to 0. However, during a transient, maintaining a constant voltage would induce some oscillations due to the line's dynamics, which are not represented in the quasi-static formulation (presented in Fig. 5) [32], [36]. This effect is noticed especially in a transmission system when there is not enough resistive effect to damp these natural oscillations. Hence a transient damping resistor (R_v) has to be added in the control. ω_f is the cut-off frequency of the high-pass filter [32], [36].

Since the connection impedance X_c (0.15 p.u.) is much smaller than for a synchronous machine in steady state (≈2.5 p.u.) [37], the voltage at the PCC is stiffly controlled. Hence, an Automatic Voltage Regulator (AVR) is not compulsory. If needed, a local reactive droop control can be added as it is shown in Fig. 7, where n_q and T_Q are the reactive droop gain and the time constant of the reactive loop, respectively.

III. IMPLEMENTATION OF THE GRID-FORMING CONTROL ON THE VSC

The previous section has presented the way to generate the reference voltage with an ideal VSC. This is the core of the control, but other functionalities have to be implemented in order to get to the proper performances. In case of a 2-level

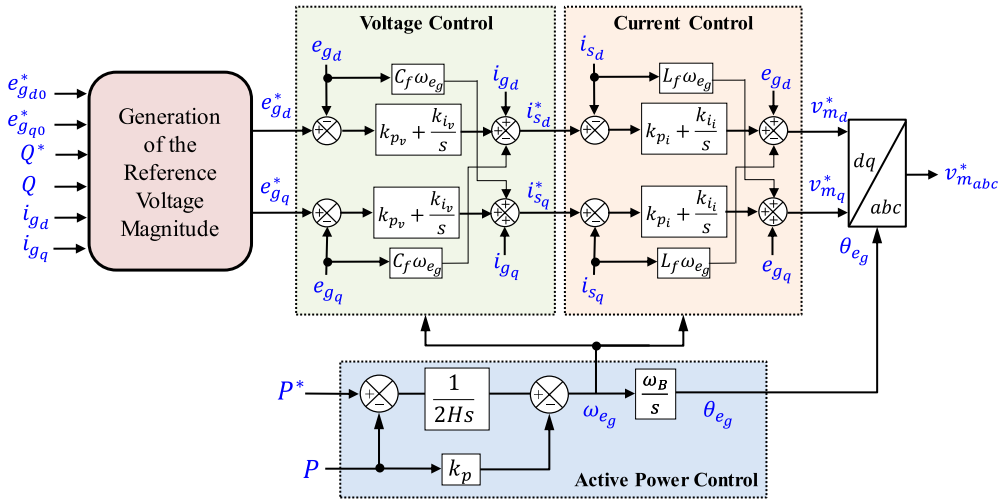

FIGURE 9. Implementation of the grid-forming 2-Level converter based on IP controller.

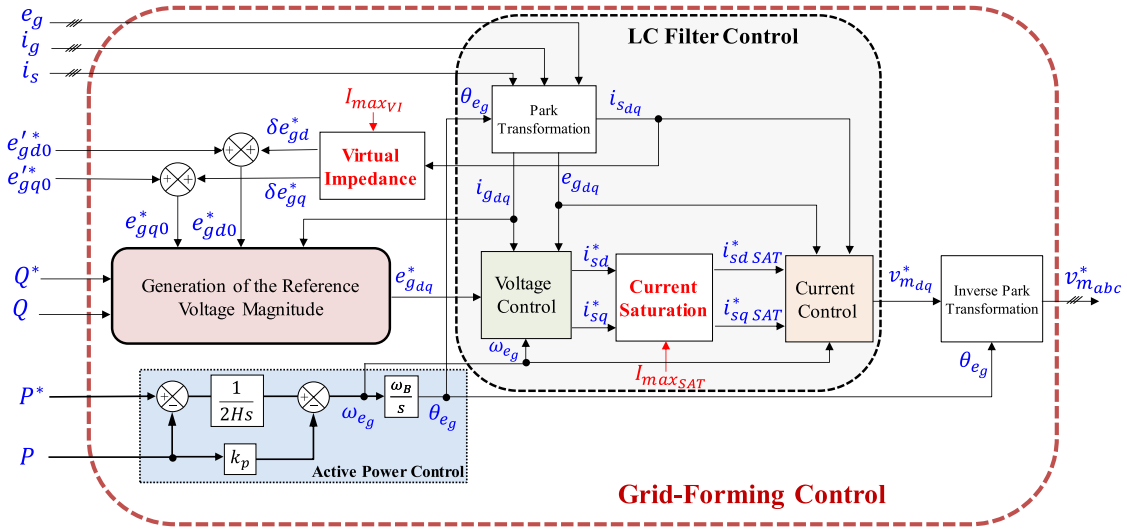

FIGURE 10. Full implementation of grid-forming control with current limitation algorithms.

VSC with an LC filter (see Fig. 8), the control has to be adjusted in order to take the internal current and voltage loops into account. Moreover, the control has to embed a current limitation algorithm in order to protect the converter against overcurrent.

A. INTEGRATION OF THE INTERNAL LOOPS

Generally, for two-level converters, an LC filter is required to eliminate the high-frequency harmonics caused by the PWM signals. When the LC filter is considered, the active power control is then achieved by acting on the phase of the voltage e_g with respect to v_g. Then, this voltage is substituted to v_m in all the previous analysis. The internal angle θ_m and frequency ω_m are replaced with θ_{e_g} and ω_{e_g} respectively. The voltage v_m^* is calculated from the voltage and current control loops [38] (see Fig. 9).

It is important to mention that the system in Fig. 8 including the control structure of Fig. 9 is a non-linear system. The non-linearity is mainly due to the calculation of the active power in the control side ($P = e_{g_d} i_{g_d} + e_{g_q} i_{g_q}$), and the evolution of the active power with respect to the angle ($P = \frac{E_g V_e}{X_c + X_g} sin\delta_{e_g}$).

B. CURRENT LIMITATION CONTROL

The core of the grid forming control is based on the generation and tracking of an AC voltage source. In case of some events in the grid some over currents may be induced in the power electronic converter. Fig. 10 shows two general approaches to implement a current limitation for the grid-forming control: the Virtual Impedance (VI) [39]–[41] and the Current Saturation Algorithm (CSA) [42]–[44]. Both algorithms are recalled:

1) CURRENT SATURATION

The saturation scheme is defined by the following function:

$$\begin{cases} i^*_{s_{dqS}} = i^*_{s_{dq}} & if\ \sqrt{i^2_{s_d}+i^2_{s_q}} < I_{\max_{SAT}} \\ i^*_{s_{dS}} = I_{\max_{SAT}} \cos\left[\arctan 2(\frac{i^*_{s_q}}{i^*_{s_d}})\right] & if\ \sqrt{i^2_{s_d}+i^2_{s_q}} \geqslant I_{\max_{SAT}} \\ i^*_{s_{qS}} = I_{\max_{SAT}} \sin\left[\arctan 2(\frac{i^*_{s_q}}{i^*_{s_d}})\right] & if\ \sqrt{i^2_{s_d}+i^2_{s_q}} \geqslant I_{\max_{SAT}} \end{cases} \tag{11}$$

$I_{max_{SAT}}$ stands for the maximum allowable current magnitude of the converter, whereas $i^*_{s_{dq_{SAT}}}$ denotes the saturated d-q currents.

2) VIRTUAL IMPEDANCE

The virtual impedance algorithm is activated only when the current exceeds its nominal value $I_n = 1p.u.$ Otherwise, it will be disabled. The expressions the virtual impedance (X_{VI} and R_{VI}) are given in (12) and (13).

$$X_{VI} = \begin{cases} k_{p_{R_{VI}}} \sigma_{X/R} \delta I & if\ \delta I > 0 \\ 0 & if\ \delta I \leqslant 0, \end{cases} \tag{12}$$

$$R_{VI} = X_{VI}/\sigma_{X/R}, \tag{13}$$

where $\delta I = I_s - I_n$ and $I_s = \sqrt{i^2_{s_d}+i^2_{s_q}}$ is the converter current magnitude. The parameters $k_{p_{R_{VI}}}$ and $\sigma_{X/R}$ are defined respectively as the virtual impedance proportional gain and the virtual impedance ratio.

The parameter $k_{p_{R_{VI}}}$ is tuned to limit the current magnitude to a suitable level $I_{\max_{VI}}$ during the overcurrent in steady state, while $\sigma_{X/R}$ ensures a good system dynamics during the overcurrent and keeps a higher X/R ratio. The tuning method of these parameters is explained in [33], [39]. When the virtual impedance is activated, the AC voltage references are given by:

$$e^*_{g_d} = e^{*\prime}_{g_d} - \delta e^*_{g_d}, \quad e^*_{g_q} = e^{*\prime}_{g_q} - \delta e^*_{g_q}, \tag{14}$$

where,

$$\delta e^*_{g_d} = R_{VI} i_{s_d} - X_{VI} i_{s_q}, \tag{15}$$

$$\delta e^*_{g_q} = R_{VI} i_{s_q} + X_{VI} i_{s_d}. \tag{16}$$

Each algorithm can be implemented independently, or both of them can be hybridized to take the benefit of each one at the same time as it is explain in [45]. The CSA allows a better current limiting during the first moments after the fault, whereas, VI cannot catch the first current peaks but it is able to guarantee a better transient stability after fault clearance compared to the CSA. Therefore, their hybridization allows an accurate current limitation and acceptable transient stability.

Until here, the main functionalities of the grid-forming control have been explained. The dynamic behavior of the converter has to be tested for different types of events (i.e. the behavior around an operating point and the performance in case of large transient).

IV. ANALYSIS OF THE PROPOSED GRID-FORMING CONTROL DYNAMICS AROUND AN OPERATING POINT

Two main events are analyzed in this section. First, a step on the active power reference is applied in order to evaluate the overall dynamics of the system and its robustness. Then, the frequency response of the system either with or without implementation of the frequency support in the converter control is studied.

A. ACTIVE POWER DYNAMICS

From Fig. 5, the dynamic of the active power around an operating point with respect to the power setpoint and the grid angle is expressed as follows:

$$\Delta P = \frac{1}{\frac{2H}{\omega_b K_c}s^2 + 2Hk_p s + 1}\Delta P^* - \frac{\frac{2H}{\omega_b}s^2}{\frac{2H}{\omega_b K_c}s^2 + 2Hk_p s + 1}\Delta\theta_g. \tag{17}$$

Equation (17) can be simplified by expressing θ_g with respect to the active power. By neglecting the losses, the active power flow between the voltage terminals v_m and v_g is the same as one between the terminals v_g and v_e. Therefore, based on (7) it can be deduced:

$$\Delta P = \frac{K_c(\Delta\omega_m - \Delta\omega_g)\omega_b}{s} = \frac{K_g(\Delta\omega_g - \Delta\omega_e)\omega_b}{s}, \tag{18}$$

where $K_g = V_g V_e / X_g$. Since the grid frequency ω_e is assumed to be constant, $\Delta\omega_e \approx 0$. Therefore, (18) can be simplified as:

$$\Delta P = \frac{K_g \omega_b}{s}\Delta\omega_g = K_g \Delta\theta_g. \tag{19}$$

By replacing $\Delta\theta_g$ in (17) by its expression in (19), the simplified active power formula derived from Fig. 5 is obtained:

$$\Delta P = \frac{1}{\frac{2H}{\omega_b}(\frac{1}{K_c}+\frac{1}{K_g})s^2 + 2Hk_p s + 1}\Delta P^*. \tag{20}$$

The damping ratio ζ and natural frequency ω_n can be calculated by following formulas:

$$\zeta = k_p\sqrt{\frac{H\omega_b K_c K_g}{2(K_c+K_g)}}, \quad \omega_n = \sqrt{\frac{\omega_b K_c K_g}{2H(K_c+K_g)}}. \tag{21}$$

From (21), the damping gain k_p can be designed to achieve the desired dynamics of the active power based on ζ and ω_n for this simplified model.

To illustrate the accuracy of the developed simplified small-signal model in (20), it is compared to the linearized state-space model in (22) and non-linear model. The linearized state-space model will also be used for robustness analysis in the next subsection.

$$\Delta\dot{\mathbf{x}} = \mathbf{A}\Delta\mathbf{x} + \mathbf{B}\Delta\mathbf{u}. \tag{22}$$

with:

$$\mathbf{x} = \begin{bmatrix} e_{gd} & e_{gq} & i_{sd} & i_{sq} & i_{gd} & i_{gq} & \delta_{eg} & \delta\omega_{eg} \\ \dots & \delta_{eg} & \zeta_d^{R_v} & \zeta_q^{R_v} & C_{vd} & C_{vq} & C_{cd} & C_{cq} \end{bmatrix}^T,$$

TABLE 1. System and control parameters.

Symbol	Quantity	Symbol	Quantity
$P_{n_1} = S_{b_1}$	1000 MW	f_n	50 Hz
$cos\phi$	1	U_{ac}	320 kV
$L_g = 10R_g$	0.333 p.u.	$I_{max_{SAT}}$	1.25 p.u.
$L_{g_1} = 10R_{g_1}$	0.833 p.u.	$\sigma_{X/R}$	5
$L_{g_2} = 10R_{g_2}$	0.556 p.u.	$I_{max_{VI}}$	1.2 p.u.
L_c	0.15 p.u.	$k_{p_{R_{VI}}}$	0.667 p.u.
R_c	0.005 p.u.	e'^{*}_{gd0}	1 p.u.
C_f	0.066 p.u.	e^{*}_{gq0}	0 p.u.
L_f	0.15 p.u.	k_{p_i}	0.73 p.u.
R_f	0.005 p.u.	k_{i_i}	1.19 p.u.
R_v	0.09 p.u.	k_{p_v}	0.52 p.u.
ω_f	60 rad/s	k_{i_v}	1.16 p.u.
n_q	0 p.u.	H	5 s
U_{dc}	640 kV	k_p	0.02

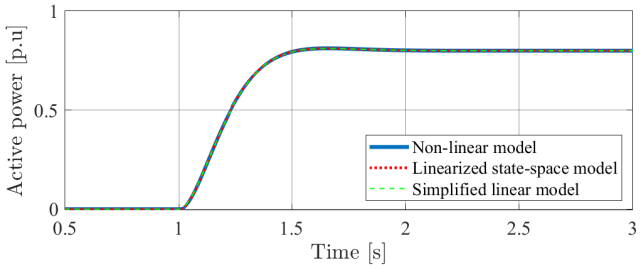

FIGURE 11. Comparison between the nonlinear full dynamic model, linearized model and proposed simplified model for SCR = 3.

$$\mathbf{u}^T = \begin{bmatrix} e'^{*}_{gd0} & V_e & P^* \end{bmatrix}.$$

- $e_{gd}, e_{gq}, i_{sd}, i_{sq}, i_{gd}, i_{gq}$: states of the LC filter.
- $\delta_{eg}, \delta\omega_{eg}$: states in the active power control loop.
- δe_g: state of the filter applied to the reactive power measurement.
- $\zeta_d^{R_v}, \zeta_q^{R_v}$: states of the transient damping resistor.
- $C_{vd}, C_{vq}, C_{cd}, C_{cq}$: corresponding states of the internal voltage and current control loops.

The **A** and **B** matrices are given in the appendix. System and control parameters are presented in Table1.

In Fig. 11, an active power set-point change of $\Delta P^* = 0.8\ p.u$ is applied. The Short Circuit Ratio (SCR) is equal to 3 for this test case (SCR $= 1/X_g^{pu}$ [46]). The obtained results show the high fidelity of the proposed linearized models in (20) and (22) compared to the non-linear model.

B. ROBUSTNESS AGAINST GRID IMPEDANCE VARIATION

To assess the robustness of the proposed control against the SCR variation, some illustrative simulations are performed in this subsection by considering the grid case of Fig. 8.

Figure 12 shows the eigenvalues trajectory of the system for both linearized state-space model and the simplified one with respect to the SCR variation. Two remarks can be derived from this result:

– The dominant modes linked to the active power dynamics from the state-space model and simplified one are matched for various SCR.

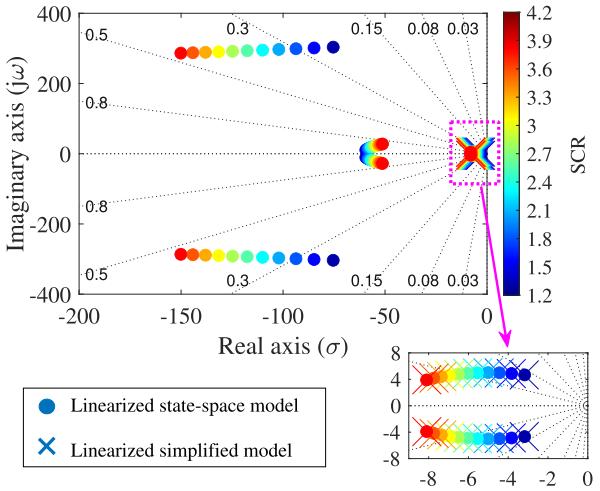

FIGURE 12. System pole map under various SCR.

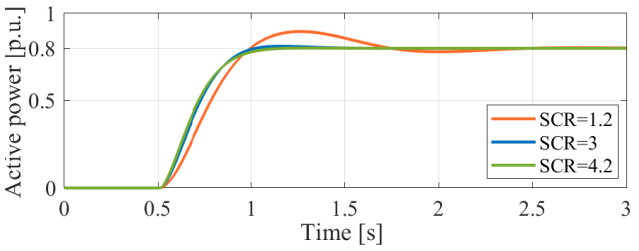

FIGURE 13. Time domain simulation under various SCR.

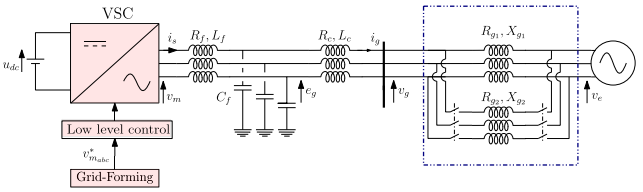

FIGURE 14. Studied system with the line-tripping scenario.

– The system is stable for a wide range of SCR.

It should be noted that SCR = 1.2 is the critical SCR that allows transferring the rated power in steady state.

Because of the high non-linearity of the system under very weak grid conditions, the stability proof stated in Fig. 12 is confirmed through time-domain simulations in Fig. 13.

The static variation of the SCR that is previously performed should be supported by the real test cases that induce a SCR change. Line tripping in power transmission systems is very likely and it leads to an increase of the interconnection impedance, and thus, a very fast decrease of the SCR.

This test case is performed on a grid impedance-switching scenario illustrated in Fig. 14. When both impedances (X_{g_1}, R_{g_1} and X_{g_2}, R_{g_2}) are connected, SCR = 3, when X_{g_2}, R_{g_2} is disconnected, the SCR decreases to 1.2. The corresponding values of these impedances are given in Table 1.

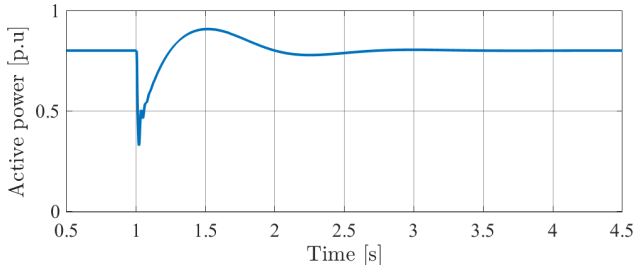

FIGURE 15. Active power response in case of line tripping.

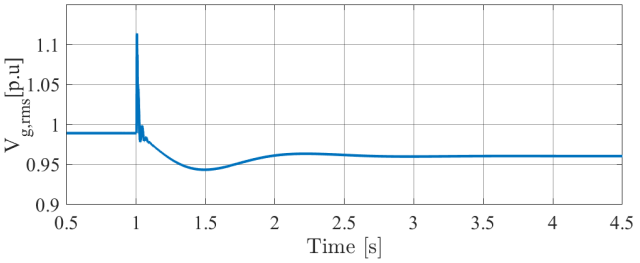

FIGURE 16. PCC voltage in case of line tripping.

In Fig. 15, P^* is initially set to 0.8 $p.u.$ and both impedances are connected. At $t = 1\ s$ the impedance X_{g_2}, R_{g_2} is tripped. The result shows that the system remains stable during this very strong disturbance and recovers its equilibrium point within one second.

The decrease of the SCR results in a decrease of the voltage magnitude at PCC (Fig. 16). However, this voltage variation is acceptable since it meets the today's grid code requirements.

C. FREQUENCY SUPPORT

In the previous sections, the VSC was connected to an infinite bus, where the frequency is assumed to be constant. However, an appropriate way to evaluate the inertial effect provided by the grid-forming converter is to test it on a variable frequency grid. The goal is to study the frequency behavior with the proposed control and to characterize its inertial contribution through theoretical analysis and the time-domain simulations.

Fig. 17 presents a VSC connected to an AC system formed by a linear resistive load and an equivalent AC grid with a variable frequency. The equivalent AC grid consists of an inertial AC voltage source in series with its impedance, which is driven by a model representing the equivalent dynamic behavior of a large system. It consists of a swing equation and a lead-lag filter, which is a simplified model of the turbine dynamics [21]. A droop control is added to support the grid frequency.

AC Grid Notations: P_g^{SI} and P_g are the active power calculated from the grid side in per-unit and SI, respectively. ω_e is the grid frequency. S_{b_2} is the base power of the equivalent AC grid. R_{SG} is the droop control gain. H_{eq}, T_N and T_D are

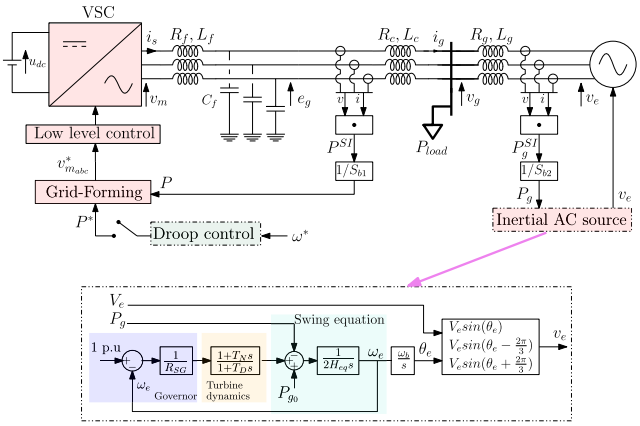

FIGURE 17. AC voltage-controlled VSC connected to an equivalent AC grid with variable frequency.

the inertia constant, the lead time constant and the lag time constant, respectively.

1) SIMPLIFIED SYSTEM MODELING

First, a simplified small-signal analytic model of the system in Fig. 17 is built. The idea is to achieve a qualitative dynamic analysis of this system in order to explain the active power and frequency behavior. The converter behavior is driven by (8). When studying the system around an operating point, it yields:

$$\begin{aligned} 2Hs\Delta\omega_m &= -\Delta P - 2Hk_p s\Delta P \\ &= -\Delta P - 2Hk_p K_c(\Delta\omega_m - \Delta\omega_g)\omega_b. \end{aligned} \quad (23)$$

The dynamics of the inertial AC source is represented by the differential equation:

$$2H_{eq}\Delta\omega_e s = \Delta P_m - \Delta P_g. \quad (24)$$

By neglecting the system losses:

$$\Delta P_g^{SI} + \Delta P^{SI} = \Delta P_{load}, \quad (25)$$

where $\Delta P_g^{SI} = S_{b_2}\Delta P_g$ and $\Delta P^{SI} = S_{b_1}\Delta P$. Converting this equation in S_{b_2} base results in:

$$\Delta P_g + \Delta P\frac{S_{b_1}}{S_{b_2}} = \frac{\Delta P_{load}}{S_{b_2}}. \quad (26)$$

To determine the dominant frequency response, it is assumed that:

$$\Delta\omega_m = \Delta\omega_g = \Delta\omega_e. \quad (27)$$

The validity of this assumption will be shown in the next subsection through time-domain simulations. By taking (27) into acount, (23) can be simplified as follows:

$$2Hs\Delta\omega_e = -\Delta P. \quad (28)$$

By putting ΔP from (28) and ΔP_g from (24) in (26), the following equation that describes the grid frequency dynamics is obtained:

$$2(H\frac{S_{b_1}}{S_{b_2}} + H_{eq})s\Delta\omega_e = \Delta P_m - \frac{\Delta P_{load}}{S_{b_2}}. \quad (29)$$

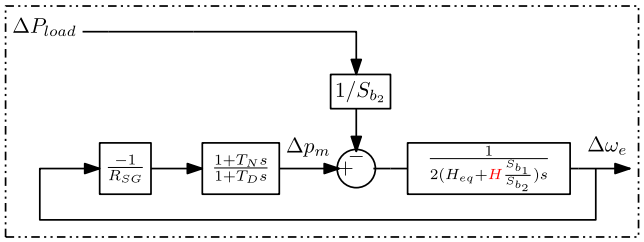

FIGURE 18. The simplified representation of the grid frequency dynamics.

TABLE 2. Parameters of the variable frequency grid.

Symbol	Quantity	Symbol	Quantity
$P_{n_1} = S_{b_1}$	500 MW	T_n	1 s
$P_{n_2} = S_{b_2}$	500 MW	T_d	6 s
R_g	0.005 p.u.	H_{eq}	5 s
L_g	0.15 p.u.	R_{SG}	0.04 p.u.
R	0.04 p.u.		

Equation (29) can be illustrated graphically by the block diagram in Fig. 18. This demonstrates the high similarity between the proposed control and the swing equation of a synchronous machine [37], [47]. Then, the dynamics of the closed loop system can be derived:

$$\Delta\omega_e = -\frac{1}{S_{b2}}\frac{R_{SG}(1+T_D s)}{1+as+bs^2}\Delta P_{load}, \tag{30}$$

where $a = T_N + 2(H_{eq} + \frac{S_{b_1}}{S_{b_2}}H)R_{SG}$ and $b = 2(H_{eq} + \frac{S_{b_1}}{S_{b_2}}H)R_{SG}T_D$. Based on (30) the Rate of Change of Frequency (RoCoF) expression for a load step ($\Delta P_{load}/s$) can be determined:

$$\lim_{s\to\infty} s^2\Delta\omega_e f_b = \frac{\Delta P_{load}}{2(H_{eq}+\frac{S_{b_1}}{S_{b_2}}H)S_{b_2}}f_b, \tag{31}$$

where f_b is the base frequency in (Hz). By putting $\Delta\omega_e$ from (28) in (30), the converter active power with respect to the load change is obtained as follows:

$$\Delta P = \frac{1}{S_{b2}}\frac{2HR_{SG}(1+T_D s)s}{1+as+bs^2}\Delta P_{load}. \tag{32}$$

2) SMALL-SIGNAL MODEL VALIDATION AND ANALYSIS

To validate the proposed simplified small-signal model (in (30) and (32)), it is compared to the non-linear model in Fig. 17 for two cases: $H = 5\ s$ and $H = 2.5\ s$. The parameters of the variable frequency AC grid are given in Table 2. Time-domain simulations are given in Fig. 18 and Fig. 19, respectively, where a 400 MW load change is applied to system.

These simulation results confirm the accuracy of the simplified model to reproduce the dominant poles. Moreover, in Fig. 19 when the load is connected, the inertial support of the grid-forming VSC based-PI controller strongly increases the VSC active power only during the transient since the

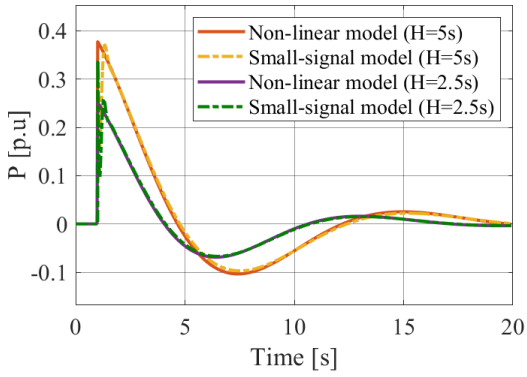

FIGURE 19. Active power dynamics with respect to a load change.

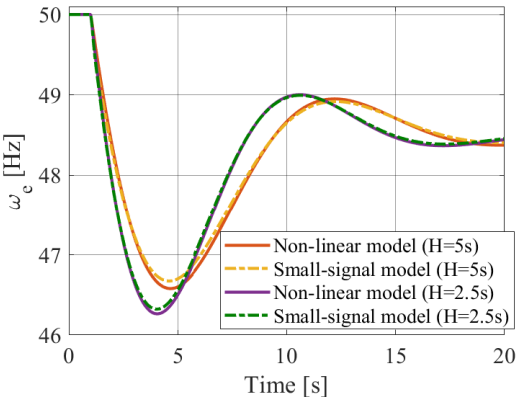

FIGURE 20. Frequency dynamics with respect to a load change.

droop control is not considered in this test case. Therefore, the load is fully handled by the AC grid in steady state. The increase of the inertia constant decreases the RoCoF as demonstrated by (31) and improves the frequency nadir as expected. (e.g., $H = 5\ s$ and $H = 2.5\ s$ correspond to RoCoF $= 1.9\ Hz/s$ and RoCoF $= 2.5\ Hz/s$, respectively).

The outer frequency droop control for the VSC depicted by the green block in Fig. 17 is an optional functionality that can be added in order to allow the power converter participating to the frequency support in steady-state. The droop control is given by the following formula:

$$P^* = \frac{1}{R}(\omega^* - \omega_m). \tag{33}$$

where ω^* and R are the frequency setpoint and droop gain of the converter, respectively. By considering (33), the simplified representative model in Fig. 18 is modified by the one in Fig. 21. This simplified model is compared to the non-linear model in Fig. 22 to prove its accuracy.

V. RESPONSE TO LARGE EVENTS AND TRANSIENT STABILITY

To address the transient stability of the proposed control with respect to a large disturbance, according to Fig. 23, a three phase bolted fault with different fault durations T_f is applied

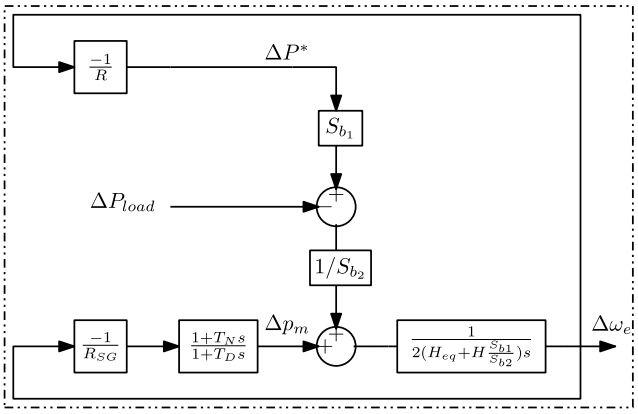

FIGURE 21. The simplified representation of the grid frequency dynamics including the droop control.

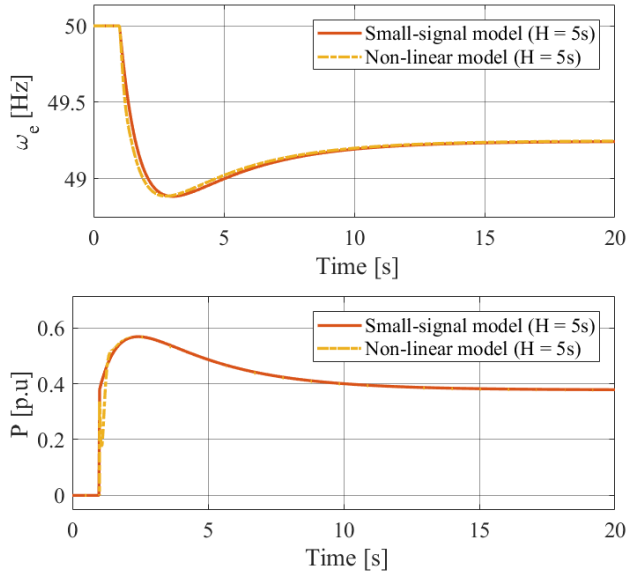

FIGURE 22. Active power and frequency dynamics with respect to a load change including the droop control ($H = 5$ s).

at the departure of one of the lines and it is cleared by tripping the faulty line, which results in a phase shift.

The results of this test case are gathered in Fig. 24. The current is well limited during the fault as expected, however, depending on the fault duration; the system may lose the synchronism. The fault clearance in 150ms results in a stable resynchronization, while, when the fault duration is higher, the angle diverges, which yields a transient instability. More details on the transient stability analysis of this phenomenon can be found in [41], [45], [48]–[50].

Referring to [45], the transient instability occurs when no dedicated control algorithm is implemented to limit the angle deviation during large transients (i.e., when the power mismatch is not controlled during the fault). Some papers propose to switch from grid-forming to the PLL-based grid-following control in order to maintain the synchronism and to ensure a transient stability [36], [51].

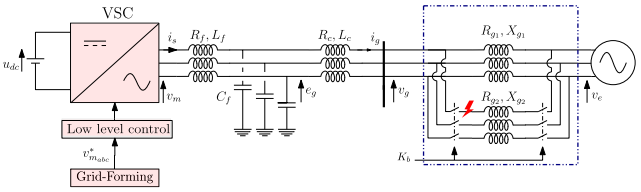

FIGURE 23. Studied system with the fault scenario.

These methods require additional fault detection algorithms and triggering conditions. Additionally, as mentioned in [36], the fault recovery based on these methods could only be achieved after a considerable re-tuning of the voltage controller and the power controller to avoid the AC voltage collapse. In the following lines, a method is proposed to enhance the transient stability with no need for a PLL or control mode switching.

Inspiring from the operation of a synchronous machine, a high inertia constant results in a better transient stability. Contrary to the SM where the inertia constant is imposed by the mechanical characteristics, the inertia constant is tunable with a grid-forming VSC, thus, an adaptive inertia algorithm is proposed in this section to limit the frequency deviation only when the current limitation algorithms are activated. In other words, the proposed algorithm does not intervene in normal operation.

The proposed solution in (34) consists in modifying the inertia constant with respect to the AC voltage reference (e'^*_{gd0}, e'^*_{gq0} in Fig. 10) generated from the virtual impedance. If the current does not reach its maximum allowable value I_{maxVI}, then, the generated d-q voltages δe^*_{gdq} from the virtual impedance are equal to zero. While, when a fault occurs and $I_s > I_{maxVI}$, the AC voltage reference is decreased to: $\sqrt{(1-\delta e^*_{gd})^2 + (\delta e^*_{gq})^2}$, where the value of e'^*_{gd0} is set to 1 and e'^*_{gq0} is set to 0. Therefore, the inertia constant is modified with the following formula:

$$H = \frac{H_0}{\sqrt{(1-\delta e^*_{gd})^2 + (\delta e^*_{gq})^2}}, \tag{34}$$

where H_0 is the initial constant in normal operation.

The contribution of the proposed algorithm to the transient stability is demonstrated through the same test case presented in Fig. 24. The simulation results including the proposed algorithm are given in Fig. 25. One can notice that the system now remains stable for both fault durations.

To demonstrate the effectiveness of the proposed control in case of another large event, a phase shift that is linked to a line reclosing is performed. The results are given in Fig. 26. In this case, initially, the line that is modeled with X_2, R_2 is assumed to be disconnected, then, it is connected at $t = 1$ s resulting in a change of the SCR from 1.2 to 3, which engender an important current transient that has been well limited thanks to the current limitation algorithm. After the disturbance, the system stably recovers its equilibrium point within 1s. Since the voltage magnitude at the PCC is not moving,

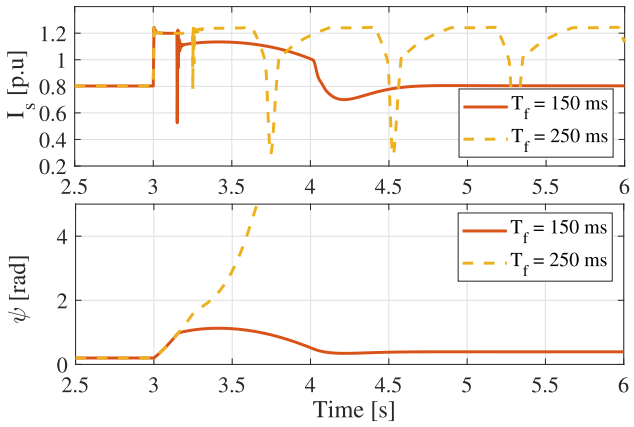

FIGURE 24. Response of the converter to the line-tripping event with time duration.

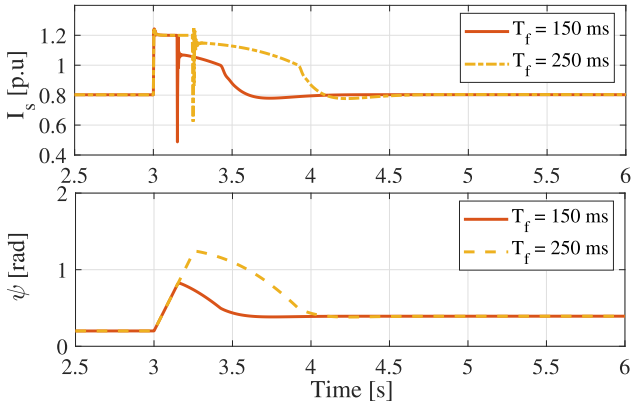

FIGURE 25. Enhancement of the transient stability through the adaptive inertia algorithm.

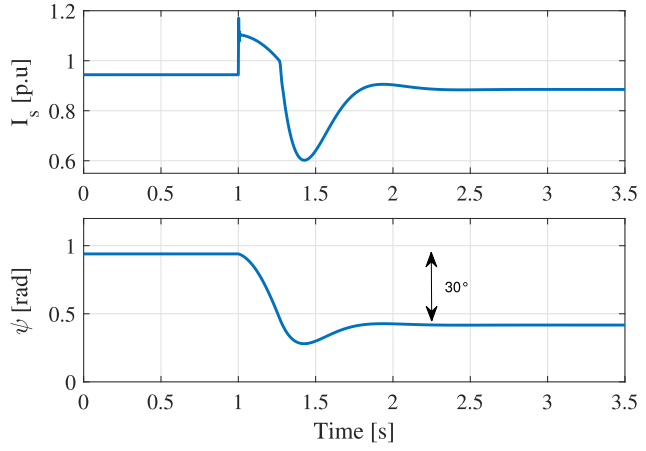

FIGURE 26. Phase shift of 30° linked to a line reclosing.

the inertia parameter is kept nearly constant as presented in (34).

VI. EXPERIMENTAL VALIDATION

The aim of this section is to validate experimentally the theoretical developments. The experimental bench is illustrated in Fig. 27.

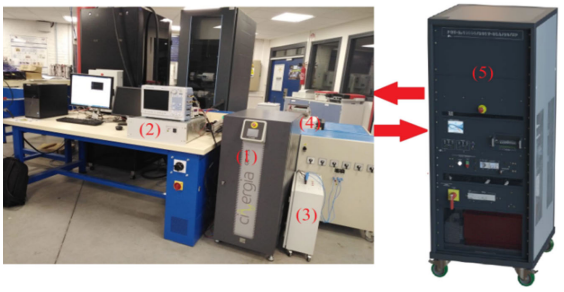

FIGURE 27. Mockup presentation.

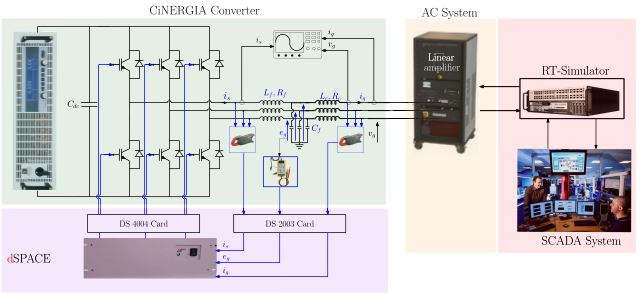

FIGURE 28. Functional scheme.

TABLE 3. Mockup parameters.

S_n	5.625 kVA	L_f	10.9 mH
I_n	10 A	L_c	10.9 mH
f_n	50 Hz	C_f	9.2 F

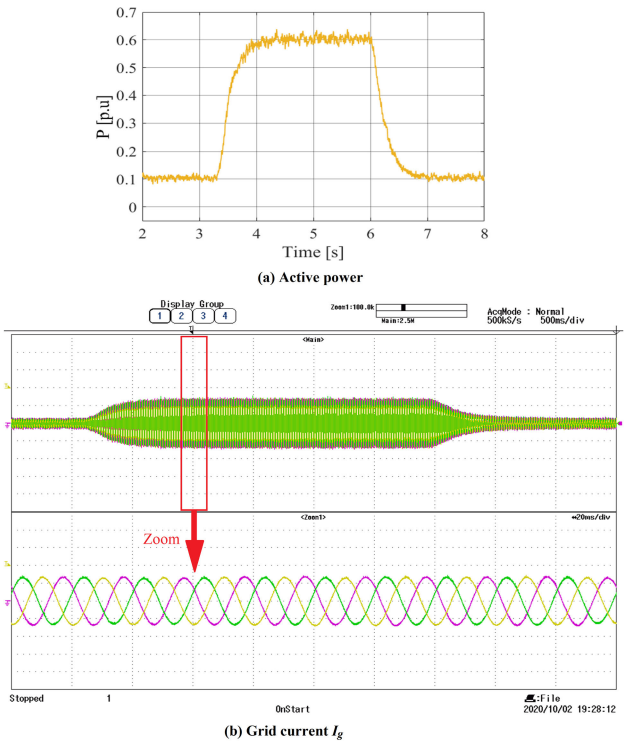

FIGURE 29. Active power change.

The 2-Level VSC (1) is supplied by an ideal 600V DC voltage source (4) and connected to a high bandwidth AC amplifier (5) through an LCL filter (3) as depicted in Fig. 28.

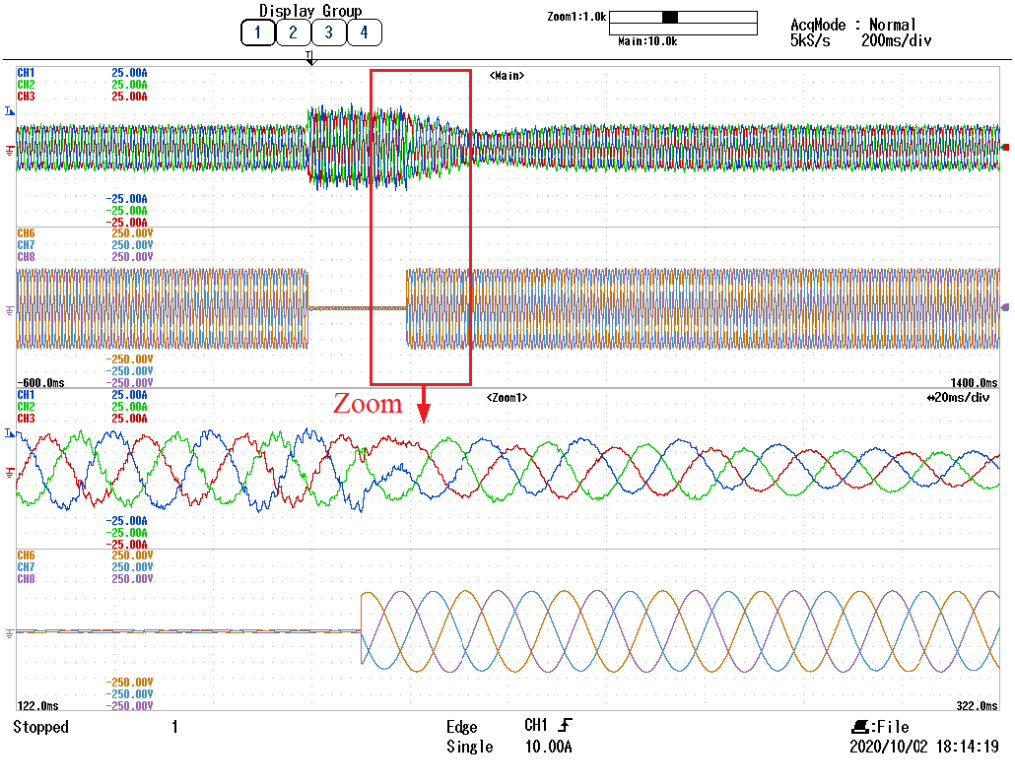

(a) 100% voltage sag.

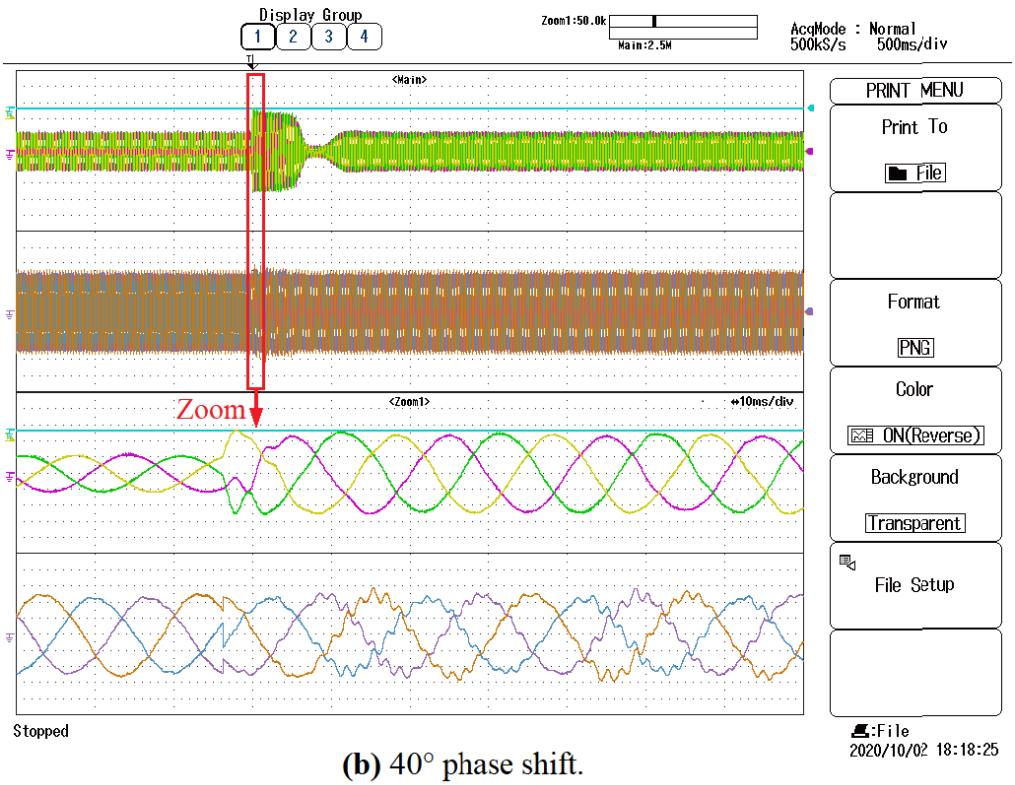

(b) 40° phase shift.

FIGURE 30. Result of experimentation - (a): 100% voltage sag, (b): 40° phase shift.

$$\mathbf{A}_{11} = \begin{Bmatrix} 0 & \omega_0\omega_b & \frac{\omega_b}{C_f} & 0 & -\frac{\omega_b}{C_f} & 0 \\ -\omega_0\omega_b & 0 & 0 & \frac{\omega_b}{C_f} & 0 & 0 \\ -\frac{\omega_b}{L_f}k_{pc}k_{pv} & -\frac{\omega_b}{L_f}k_{pc}C_f\omega_0 & -\left(\frac{\omega_b}{L_f}k_{pc}+\frac{R_f\omega_b}{L_f}\right) & 0 & \frac{\omega_b}{L_f}k_{pc} & 0 \\ \frac{\omega_b}{L_f}k_{pc}C_f\omega_0 & -\frac{\omega_b}{L_f}k_{pc}k_{pv} & 0 & -\left(\frac{\omega_b}{L_f}k_{pc}+\frac{R_f\omega_b}{L_f}\right) & 0 & \frac{\omega_b}{L_f}k_{pc} \\ \frac{\omega_b}{L_C+L_g} & 0 & 0 & 0 & -\frac{(R_c+R_g)\,\omega_b}{L_C+L_g} & \omega_0\omega_b \\ 0 & \frac{\omega_b}{L_C+L_g} & 0 & 0 & -\omega_0\omega_b & -\frac{(R_c+R_g)\,\omega_b}{L_C+L_g} \end{Bmatrix}_{6\times6}$$

$$\mathbf{A}_{12} = \begin{Bmatrix} 0 & 0 & 0 & 0 & 0 & 0 & 0 & 0 & 0 \\ 0 & 0 & 0 & 0 & 0 & 0 & 0 & 0 & 0 \\ 0 & \frac{\omega_b}{L_f}k_{pc}k_{pv} & \frac{\omega_b}{L_f}k_{pc}k_{i_v} & 0 & 0 & \frac{\omega_b}{L_f}k_{ic} & 0 & \frac{\omega_b}{L_f}k_{pc}k_{pv} & 0 \\ 0 & 0 & 0 & \frac{\omega_b}{L_f}k_{pc}k_{i_v} & \frac{\omega_b}{L_f}k_{pc}k_{i_v} & 0 & \frac{\omega_b}{L_f}k_{ic} & 0 & \frac{\omega_b}{L_f}k_{pc}k_{pv} \\ \frac{V_e\sin\delta_{eg0}\omega_b}{L_C+L_g} & 0 & 0 & 0 & 0 & 0 & 0 & 0 & 0 \\ \frac{V_e\cos\delta_{eg0}\omega_b}{L_C+L_g} & 0 & 0 & 0 & 0 & 0 & 0 & 0 & 0 \end{Bmatrix}_{6\times9}$$

$$\mathbf{A}_{21} = \begin{Bmatrix} -k_pI_{gd0} & -k_pI_{gq0} & 0 & 0 & -k_pE_{gd0} & 0 \\ -\frac{I_{gd0}}{2H} & -\frac{I_{gq0}}{2H} & 0 & 0 & -\frac{E_{gd0}}{2H} & 0 \\ \frac{n_qI_{gq_0}}{T_Q} & -\frac{n_qI_{gd_0}}{T_Q} & 0 & 0 & 0 & \frac{n_qE_{gd_0}}{T_Q} \\ -1 & 0 & 0 & 0 & 0 & 0 \\ 0 & -1 & 0 & 0 & 0 & 0 \\ -k_{pv} & -C_f\omega_0 & -1 & 0 & 1 & 0 \\ C_f\omega_0 & -k_{pv} & 0 & -1 & 0 & 1 \\ -\frac{R_V\omega_b}{L_C+L_g} & 0 & 0 & 0 & \frac{R_v\left(R_c+R_g\right)\omega_b}{L_C+L_g} & -R_v\omega_0\omega_b \\ 0 & -\frac{R_V\omega_b}{L_C+L_g} & 0 & 0 & R_v\omega_0\omega_b & \frac{R_v\left(R_c+R_g\right)\omega_b}{L_C+L_g} \end{Bmatrix}_{9\times6}$$

$$\mathbf{A}_{22} = \begin{Bmatrix} 0 & \omega_b & 0 & 0 & 0 & 0 & 0 & 0 & 0 \\ 0 & 0 & 0 & 0 & 0 & 0 & 0 & 0 & 0 \\ 0 & 0 & \frac{-1}{T_Q} & 0 & 0 & 0 & 0 & 0 & 0 \\ 0 & 0 & 1 & 0 & 0 & 0 & 0 & 1 & 0 \\ 0 & 0 & 0 & 0 & 0 & 0 & 0 & 0 & 1 \\ 0 & 0 & k_{p_v} & k_{i_v} & 0 & 0 & 0 & k_{p_v} & 0 \\ 0 & 0 & 0 & 0 & 0 & 0 & 0 & 0 & k_{p_v} \\ -\frac{R_vV_e\sin\delta_{eg0}\omega_b}{L_C+L_g} & 0 & 0 & 0 & 0 & 0 & 0 & -\omega_f & 0 \\ -\frac{R_vV_e\cos\delta_{eg0}\omega_b}{L_C+L_g} & 0 & 0 & 0 & 0 & 0 & 0 & 0 & -\omega_f \end{Bmatrix}_{9\times9}$$

$$\mathbf{B}^{\mathbf{T}} = \begin{Bmatrix} 0 & 0 & 0 & 0 & 0 & 0 & 0 & 0 & 0 & 0 & 0 & 0 & \omega_f & 0 \\ 0 & 0 & 0 & 0 & -\frac{\cos\delta_{eg0}\omega_b}{L_C+L_g} & \frac{\sin\delta_{eg0}\omega_b}{L_C+L_g} & 0 & 0 & 0 & 0 & 0 & 0 & 0 & 0 & 0 \\ 0 & 0 & 0 & 0 & 0 & 0 & 0 & \frac{1}{2H} & 0 & 0 & 0 & 0 & 0 & 0 & 0 \end{Bmatrix}_{3\times15}$$

Table 3 presents the mockup parameters. The amplifier is used to emulate the AC system (i.e.; 300V ph-ph) as well as to generate the events discussed in this paper (i.e.; 100% voltage sag emulating a 3-phase bolted fault and a phase shift). The 2-Level VSC is controlled with a dSPACE dS1005 (2) with a 40 μs time step. The switching frequency of the converter is $f_{sw} = 10\ kHz$.

The electrical quantities displayed in experimentation are respectively the grid voltages v_g in (abc) frame, the VSC output current I_s in (abc) frame, the grid current I_g in (abc) frame and the active power. Three test cases are performed:

- 0.5 p.u. active power change.
- A 100% grid voltage sag.
- A phase shift of 40°

A. ACTIVE POWER CHANGE

At $t = t_0$, $P^* = 0.1\ p.u$, then, a 0.5 $p.u$ power step is applied. Fig. 29 shows the active power dynamics with the proposed control. The active power tracks its reference without overshoot within 600ms, which is very close to what has been specified in Fig. 11. A difference between the simulation and the experimentation can simply be explained by the fact that the X/R ratio in a small-scale converter is smaller, which affects a little bit the dynamic performance of the system.

B. 100% VOLTAGE SAG

Initially, $P^* = 0.7\ p.u$. Subsequently, a 400 ms voltage sag is applied as shown in Fig. 30-a. When the fault occurs, the AC voltage drop induces an increase in the VSC output current, which is limited beyond its maximum allowable current magnitude, 1.2 p.u (12 A). Once the fault is cleared, the system stably recovers its equilibrium point.

C. 40° PHASE SHIFT

In this subsection, the power reference is first set to $P^* = 0.5\ p.u$ and a phase-shift of 40° is then applied, as illustrated in Fig. 30-b. The current rises to its maximum allowable value, then, the system recovers its equilibrium point depending on the dynamics of the controller.

VII. CONCLUSION

In this paper, a grid-forming control strategy has been proposed and its effectiveness under different grid test cases has been demonstrated. To analyze the dynamic performance of the proposed control, a small signal model has been developed and verified. Moreover, the transient stability was addressed and an adaptive inertia constant algorithm has been implemented in order to guarantee the system stability against large events that may occur in power system. It can be said that this simple PI controller with an adaption of the parameters during a short circuit is extremely robust and it meets the main requirements asked by the transmission system operators. Other perspectives consist in extending the proposed control for an MMC topology and testing it under unbalanced faulty conditions as well.

APPENDIX

The $\mathbf{A}$ and $\mathbf{B}$ matrices of the linearized state-space model are given in the following lines:

$$\Delta\dot{\mathbf{x}} = \begin{Bmatrix} \mathbf{A}_{11} & \mathbf{A}_{12} \\ \mathbf{A}_{21} & \mathbf{A}_{22} \end{Bmatrix} \Delta\mathbf{x} + \mathbf{B}\Delta\mathbf{u}, \tag{35}$$

where, $\mathbf{A}_{11}$, $\mathbf{A}_{12}$, $\mathbf{A}_{21}$, $\mathbf{A}_{22}$, and $\mathbf{B}^{\mathbf{T}}$ as shown at the bottom of the previous page.

REFERENCES

[1] European Union, "Commission Regulation (Eu) 2016/631," *Off. J. Eur. Union*, no. 14, p. 68, Apr. 2016.
[2] A. Adib, B. Mirafzal, X. Wang, and F. Blaabjerg, "On stability of voltage source inverters in weak grids," *IEEE Access*, vol. 6, pp. 4427–4439, 2018, doi: 10.1109/ACCESS.2017.2788818.
[3] A. Ulbig, T. S. Borsche, and G. Andersson, "Impact of low rotational inertia on power system stability and operation," 2013, *arXiv:1312.6435*. [Online]. Available: http://arxiv.org/abs/1312.6435
[4] ENTSO-E. (Mar. 2017). *High Penetration of Power Electronic Interfaced Power Sources (HPoPEIPS)*. [Online]. Available: https://consultations.entsoe.eu/system-development/entso-e-connection-codes-implementation-guidance-d-3
[5] J. Liu, Y. Miura, and T. Ise, "Comparison of dynamic characteristics between virtual synchronous generator and droop control in inverter-based distributed generators," *IEEE Trans. Power Electron.*, vol. 31, no. 5, pp. 3600–3611, May 2016, doi: 10.1109/TPEL.2015.2465852.
[6] B. Li and L. Zhou, "Power decoupling method based on the diagonal compensating matrix for VSG-controlled parallel inverters in the microgrid," *Energies*, vol. 10, no. 12, p. 2159, Dec. 2017, doi: 10.3390/en10122159.
[7] J. Driesen and K. Visscher, "Virtual synchronous generators," in *Proc. IEEE Power Energy Soc. Gen. Meeting-Convers. Del. Electr. Energy 21st Century*, Jul. 2008, pp. 1–3, doi: 10.1109/PES.2008.4596800.
[8] Q.-C. Zhong and G. Weiss, "Synchronverters: Inverters that mimic synchronous generators," *IEEE Trans. Ind. Electron.*, vol. 58, no. 4, pp. 1259–1267, Apr. 2011, doi: 10.1109/TIE.2010.2048839.
[9] Q.-C. Zhong, P.-L. Nguyen, Z. Ma, and W. Sheng, "Self-synchronized synchronverters: Inverters without a dedicated synchronization unit," *IEEE Trans. Power Electron.*, vol. 29, no. 2, pp. 617–630, Feb. 2014, doi: 10.1109/TPEL.2013.2258684.
[10] Z. Ma, Q.-C. Zhong, and J. D. Yan, "Synchronverter-based control strategies for three-phase PWM rectifiers," in *Proc. 7th IEEE Conf. Ind. Electron. Appl. (ICIEA)*, Jul. 2012, pp. 225–230, doi: 10.1109/ICIEA.2012.6360727.
[11] R. Rosso, J. Cassoli, G. Buticchi, S. Engelken, and M. Liserre, "Robust stability analysis of LCL filter based synchronverter under different grid conditions," *IEEE Trans. Power Electron.*, vol. 34, no. 6, pp. 5842–5853, Jun. 2019, doi: 10.1109/TPEL.2018.2867040.
[12] R. Rosso, S. Engelken, and M. Liserre, "Robust stability analysis of synchronverters operating in parallel," *IEEE Trans. Power Electron.*, vol. 34, no. 11, pp. 11309–11319, Nov. 2019, doi: 10.1109/TPEL.2019.2896707.
[13] W. Wu, Y. Chen, A. Luo, L. Zhou, X. Zhou, L. Yang, Y. Dong, and J. M. Guerrero, "A virtual inertia control strategy for DC microgrids analogized with virtual synchronous machines," *IEEE Trans. Ind. Electron.*, vol. 64, no. 7, pp. 6005–6016, Jul. 2017, doi: 10.1109/TIE.2016.2645898.
[14] S. D'Arco and J. A. Suul, "Equivalence of virtual synchronous machines and frequency-droops for converter-based MicroGrids," *IEEE Trans. Smart Grid*, vol. 5, no. 1, pp. 394–395, Jan. 2014, doi: 10.1109/TSG.2013.2288000.
[15] Y. Chen, R. Hesse, D. Turschner, and H.-P. Beck, "Comparison of methods for implementing virtual synchronous machine on inverters," in *Proc. Int. Conf. Renew. Energy Power Qual. J.*, Apr. 2012, pp. 734–739, doi: 10.24084/repqj10.453.
[16] H.-P. Beck and R. Hesse, "Virtual synchronous machine," in *Proc. 9th Int. Conf. Electr. Power Qual. Utilisation*, Oct. 2007, pp. 1–6, doi: 10.1109/EPQU.2007.4424220.
[17] Y. Chen, R. Hesse, D. Turschner, and H.-P. Beck, "Improving the grid power quality using virtual synchronous machines," in *Proc. Int. Conf. Power Eng., Energy Electr. Drives*, May 2011, pp. 1–6, doi: 10.1109/PowerEng.2011.6036498.

[18] S. D'Arco, J. A. Suul, and O. B. Fosso, "A virtual synchronous machine implementation for distributed control of power converters in smartgrids," *Electr. Power Syst. Res.*, vol. 122, pp. 180–197, May 2015, doi: 10.1016/j.epsr.2015.01.001.

[19] M. Yu, A. J. Roscoe, C. D. Booth, A. Dysko, R. Ierna, J. Zhu, and H. Urdal, "Use of an inertia-less virtual synchronous machine within future power networks with high penetrations of converters," in *Proc. Power Syst. Comput. Conf. (PSCC)*, Jun. 2016, pp. 1–7, doi: 10.1109/PSCC.2016.7540926.

[20] R. Hesse, D. Turschner, and H.-P. Beck, "Micro grid stabilization using the virtual synchronous machine (VISMA)," *Renew. Energy Power Qual. J.*, vol. 1, no. 7, pp. 676–681, Apr. 2009, doi: 10.24084/repqj07.472.

[21] T. Qoria, F. Gruson, F. Colas, G. Denis, T. Prevost, and X. Guillaud, "Inertia effect and load sharing capability of grid forming converters connected to a transmission grid," in *Proc. 15th IET Int. Conf. AC DC Power Transmiss. (ACDC)*, Coventry, U.K., 2019, p. 6.

[22] N. Soni, S. Doolla, and M. C. Chandorkar, "Improvement of transient response in microgrids using virtual inertia," *IEEE Trans. Power Del.*, vol. 28, no. 3, pp. 1830–1838, Jul. 2013, doi: 10.1109/TPWRD.2013.2264738.

[23] J. Zhu, C. D. Booth, G. P. Adam, A. J. Roscoe, and C. G. Bright, "Inertia emulation control strategy for VSC-HVDC transmission systems," *IEEE Trans. Power Syst.*, vol. 28, no. 2, pp. 1277–1287, May 2013, doi: 10.1109/TPWRS.2012.2213101.

[24] D. Groß, M. Colombino, J.-S. Brouillon, and F. Dörfler, "The effect of transmission-line dynamics on grid-forming dispatchable virtual oscillator control," 2018, *arXiv:1802.08881*. [Online]. Available: http://arxiv.org/abs/1802.08881

[25] M. Ali, A. Sahoo, H. I. Nurdin, J. Ravishankar, and J. E. Fletcher, "On the power sharing dynamics of parallel-connected virtual oscillator-controlled and droop-controlled inverters in an AC microgrid," in *Proc. IECON-45th Annu. Conf. IEEE Ind. Electron. Soc.*, Lisbon, Portugal, Oct. 2019, pp. 3931–3936, doi: 10.1109/IECON.2019.8927510.

[26] Z. Shi, H. I. Nurdin, J. E. Fletcher, and J. Li, "Similarities between virtual oscillator controlled and droop controlled three-phase inverters," in *Proc. IEEE 18th Int. Power Electron. Motion Control Conf. (PEMC)*, Budapest, Hungary, Aug. 2018, pp. 434–439, doi: 10.1109/EPEPEMC.2018.8521928.

[27] M. Colombino, D. Groß, J.-S. Brouillon, and F. Dörfler, "Global phase and magnitude synchronization of coupled oscillators with application to the control of grid-forming power inverters," 2017, *arXiv:1710.00694*. [Online]. Available: http://arxiv.org/abs/1710.00694

[28] D. Raisz, T. T. Thai, and A. Monti, "Power control of virtual oscillator controlled inverters in grid-connected mode," *IEEE Trans. Power Electron.*, vol. 34, no. 6, pp. 5916–5926, Jun. 2019, doi: 10.1109/TPEL.2018.2868996.

[29] T. T. Thai, D. Raisz, A. Monti, F. Ponci, and A. Ahmadifar, "Voltage harmonic reduction using virtual oscillator based inverters in islanded microgrids," in *Proc. 18th Int. Conf. Harmon. Qual. Power (ICHQP)*, Ljubljana, Slovenia, May 2018, pp. 1–6, doi: 10.1109/ICHQP.2018.8378896.

[30] M. Z. Jacobson, M. A. Delucchi, M. A. Cameron, and B. V. Mathiesen, "Matching demand with supply at low cost in 139 countries among 20 world regions with 100% intermittent wind, water, and sunlight (WWS) for all purposes," *Renew. Energy*, vol. 123, pp. 236–248, Aug. 2018, doi: 10.1016/j.renene.2018.02.009.

[31] M. Ashabani, F. D. Freijedo, S. Golestan, and J. M. Guerrero, "Inducverters: PLL-less converters with auto-synchronization and emulated inertia capability," *IEEE Trans. Smart Grid*, vol. 7, no. 3, pp. 1660–1674, May 2016, doi: 10.1109/TSG.2015.2468600.

[32] T. Qoria, Q. Cossart, C. Li, X. Guillaud, F. Gruson, and X. Kestelyn, "Deliverable 3.2: Local control and simulation tools for large transmission systems," Migrate Project WP3, Paris, France, 2018, p. 89.

[33] G. Denis, "From grid-following to grid-forming: The new strategy to build 100% power-electronics interfaced transmission system with enhanced transient behavior," Ph.D. dissertation, Ecole centrale de Lille, Villeneuve-d'Ascq, France, 2017.

[34] F. Milano, F. Dorfler, G. Hug, D. J. Hill, and G. Verbic, "Foundations and challenges of low-inertia systems (Invited Paper)," in *Proc. Power Syst. Comput. Conf. (PSCC)*, Dublin, Ireland, Jun. 2018, pp. 1–25, doi: 10.23919/PSCC.2018.8450880.

[35] E. Rokrok, T. Qoria, A. Bruyere, B. Francois, and X. Guillaud, "Classification and dynamic assessment of droop-based grid-forming control schemes: Application in HVDC systems," *Electr. Power Syst. Res.*, vol. 189, Dec. 2020, Art. no. 106765, doi: 10.1016/j.epsr.2020.106765.

[36] L. Zhang, L. Harnefors, and H.-P. Nee, "Power-synchronization control of grid-connected voltage-source converters," *IEEE Trans. Power Syst.*, vol. 25, no. 2, pp. 809–820, May 2010, doi: 10.1109/TPWRS.2009.2032231.

[37] P. Kundur, *Power System Stability and Control*. New York, NY, USA: McGraw-Hill, 1994.

[38] T. Qoria, F. Gruson, F. Colas, X. Guillaud, M.-S. Debry, and T. Prevost, "Tuning of cascaded controllers for robust grid-forming voltage source converter," in *Proc. Power Syst. Comput. Conf. (PSCC)*, Jun. 2018, pp. 1–7, doi: 10.23919/PSCC.2018.8443018.

[39] A. D. Paquette and D. M. Divan, "Virtual impedance current limiting for inverters in microgrids with synchronous generators," *IEEE Trans. Ind. Appl.*, vol. 51, no. 2, pp. 1630–1638, Mar. 2015, doi: 10.1109/TIA.2014.2345877.

[40] X. Lu, J. Wang, J. M. Guerrero, and D. Zhao, "Virtual-impedance-based fault current limiters for inverter dominated AC microgrids," *IEEE Trans. Smart Grid*, vol. 9, no. 3, pp. 1599–1612, May 2018, doi: 10.1109/TSG.2016.2594811.

[41] T. Qoria, F. Gruson, F. Colas, G. Denis, T. Prevost, and X. Guillaud, "Critical clearing time determination and enhancement of grid-forming converters embedding virtual impedance as current limitation algorithm," *IEEE J. Emerg. Sel. Topics Power Electron.*, vol. 8, no. 2, pp. 1050–1061, Jun. 2020, doi: 10.1109/JESTPE.2019.2959085.

[42] N. Bottrell and T. C. Green, "Comparison of current-limiting strategies during fault ride-through of inverters to prevent latch-up and wind-up," *IEEE Trans. Power Electron.*, vol. 29, no. 7, pp. 3786–3797, Jul. 2014, doi: 10.1109/TPEL.2013.2279162.

[43] M. G. Taul, X. Wang, P. Davari, and F. Blaabjerg, "Current limiting control with enhanced dynamics of grid-forming converters during fault conditions," *IEEE J. Emerg. Sel. Topics Power Electron.*, vol. 8, no. 2, pp. 1062–1073, Jun. 2020, doi: 10.1109/JESTPE.2019.2931477.

[44] Q.-C. Zhong and G. C. Konstantopoulos, "Current-limiting droop control of grid-connected inverters," *IEEE Trans. Ind. Electron.*, vol. 64, no. 7, pp. 5963–5973, Jul. 2017, doi: 10.1109/TIE.2016.2622402.

[45] T. Qoria, F. Gruson, F. Colas, X. Kestelyn, and X. Guillaud, "Current limiting algorithms and transient stability analysis of grid-forming VSCs," *Electr. Power Syst. Res.*, vol. 189, Dec. 2020, Art. no. 106726, doi: 10.1016/j.epsr.2020.106726.

[46] E. Rokrok, T. Qoria, A. Bruyere, B. Francois, and X. Guillaud, "Effect of using PLL-based grid-forming control on active power dynamics under various SCR," in *Proc. IECON-45th Annu. Conf. IEEE Ind. Electron. Soc.*, vol. 1, Oct. 2019, pp. 4799–4804, doi: 10.1109/IECON.2019.8927648.

[47] T. Qoria, "Grid-forming control to achieve a 100% power electronics interfaced power transmission systems," Ph.D. dissertation, ENSAM, Paris, France, 2020.

[48] L. Huang, H. Xin, Z. Wang, L. Zhang, K. Wu, and J. Hu, "Transient stability analysis and control design of droop-controlled voltage source converters considering current limitation," *IEEE Trans. Smart Grid*, vol. 10, no. 1, pp. 578–591, Jan. 2019, doi: 10.1109/TSG.2017.2749259.

[49] H. Xin, L. Huang, L. Zhang, Z. Wang, and J. Hu, "Synchronous instability mechanism of P-f droop-controlled voltage source converter caused by current saturation," *IEEE Trans. Power Syst.*, vol. 31, no. 6, pp. 5206–5207, Nov. 2016, doi: 10.1109/TPWRS.2016.2521325.

[50] X. Wang, M. G. Taul, H. Wu, Y. Liao, F. Blaabjerg, and L. Harnefors, "Grid-synchronization stability of converter-based resources—An overview," *IEEE Open J. Ind. Appl.*, vol. 1, pp. 115–134, 2020, doi: 10.1109/OJIA.2020.3020392.

[51] M. Ndreko, S. Rüberg, and W. Winter, "Grid forming control scheme for power systems with up to 100% power electronic interfaced generation: A case study on great Britain test system," *IET Renew. Power Gener.*, vol. 14, no. 8, pp. 1268–1281, Jun. 2020, doi: 10.1049/iet-rpg.2019.0700.

TAOUFIK QORIA received the M.S. degree in electrical engineering for sustainable development from the Lille 1 University of Science and Technology, Villeneuve d'Ascq, France, in 2016. He is currently pursuing the Ph.D. degree with the ENSAM ParisTech in the Laboratory of Electrical Engineering and the Power Electronics of Lille (L2EP), Lille, France. Since 2016, he has been working on the modeling and control of the power inverters in HVDC and HVAC applications. He is also working as a Contractual Researcher with the Ecole Centrale de Lille. His current research interest includes the massive integration of power electronic devices in power transmission systems.

EBRAHIM ROKROK (Student Member, IEEE) received the B.Sc. and M.Sc. degrees in electrical engineering from the Isfahan University of Technology, in 2014 and 2016, respectively. He is currently pursuing the Ph.D. degree with the Ecole Centrale de Lille, Laboratory of Electrical Engineering and the Power Electronics of Lille (L2EP), Lille, France. This Ph.D. is supported by the project "HVDC Inertia Provision" (HVDC Pro), financed by the ENERGIX Program of the Research Council of Norway (RCN). His research interests include modeling and control of the power converters for HVDC applications.

ANTOINE BRUYERE (Member, IEEE) received the Ph.D. degree in electrical engineering in 2009. He spent ten years in automotive industry, at the Valeo Powertrain Electronics Product Group, working as an Expert in automotive electrification. In 2016, he became an Assistant Professor at the Centrale Lille Institute, Laboratory of Electrical Engineering of Lille. His research interests include renewable energy integration on power-grid, using power-electronics converters.

BRUNO FRANÇOIS (Senior Member, IEEE) is currently a Full Professor with the Centrale Lille Institute and the Laboratory of Electrical Engineering and Power Electronics Laboratory, Lille. His research interests include the advanced energy management of power systems, architectures and control systems of future electrical networks, smart grids, and uncertainty impact in operation of electrical systems.

XAVIER GUILLAUD (Member, IEEE) has been working as a Professor with the Lille Laboratory of Electrical Engineering and Power Electronics (L2EP), Lille, France, since 2002. First, he worked on the modeling and control of power electronic systems. Then, he studied the integration of distributed generation and renewable energy in power systems. Nowadays, he is studying the high-voltage power electronic converters in transmission systems. He is leading the development of an experimental facility composed of actual power electronic converters interacting with virtual grids modeled in a real-time simulator. He is involved in several projects in the field of power electronics including European grid projects and different projects with French companies.